

Numerical analysis of a red blood cell flowing through a thin micropore

Toshihiro Omori,* Haruki Hosaka, Yohsuke Imai, Takami Yamaguchi, and Takuji Ishikawa

Department of Bioengineering and Robotics, Tohoku University, Aoba 6-6-01, Aramaki, Sendai, Miyagi, Japan

(Received 26 October 2013; published 13 January 2014)

Red blood cell (RBC) deformability plays a key role in microcirculation, especially in vessels that have diameters even smaller than the nominal cell size. In this study, we numerically investigate the dynamics of an RBC in a thin micropore. The RBC is modeled as a capsule with a thin hyperelastic membrane. In a numerical simulation, we employ a boundary element method for fluid mechanics and a finite element method for membrane mechanics. The resulting RBC deformation towards the flow direction is suppressed considerably by increased cytoplasm viscosity, whereas the gap between the cell membrane and solid wall becomes smaller with higher cytoplasm viscosity. We also measure the transit time of the RBC and find that nondimensional transit time increases nonlinearly with respect to the viscosity ratio, whereas it is invariant to the capillary number. In conclusion, cytoplasmic viscosity plays a key role in the dynamics of an RBC in a thin pore. The results of this study will be useful for designing a microfluidic device to measure cytoplasmic viscosity.

DOI: [10.1103/PhysRevE.89.013008](https://doi.org/10.1103/PhysRevE.89.013008)

PACS number(s): 47.63.-b, 47.11.-j, 46.15.-x

I. INTRODUCTION

Red blood cells (RBCs) have no nucleus and consist of a nearly Newtonian hemoglobin solution in the membrane. The cell membrane is constructed by a lipid bilayer and a supportive cytoskeleton of proteins, which allow for the large elastic deformation of the membrane. Because of membrane deformability RBCs can pass through narrow capillaries. Flowing RBCs strongly affect the rheology and mass transport of blood, and the properties of RBCs have been investigated by many researchers over the past 50 years.

Because the oxygen exchange between the blood and tissues occurs mainly in microcirculation, RBC motion in a narrow capillary has been investigated analytically [1], numerically [2,3], and experimentally [4,5]. Secomb *et al.* [1] investigated the flow of an RBC analytically in a narrow cylindrical tube with an inside diameter of up to $8\ \mu\text{m}$. The cell shape was assumed to be axisymmetric and lubrication theory was used to describe the gap flow between the cells and the vessel wall. A full three-dimensional numerical simulation of RBC motion in a narrow tube was also conducted by Pozrikidis [3]. He reported distributions of membrane tension and the results were compared to initially spherical and oblate ellipsoidal capsules.

A capillary flow not only has physiological relevance, but it can also be used to measure the mechanical properties of cell membranes. In a long capillary, the motion of an RBC reaches a steady state when the flow is sufficiently developed, and the cell shape is determined only by the flow rate and membrane elastic modulus. Hu *et al.* [6], for example, investigated capsule motion in a narrow capillary numerically. They evaluated the membrane elastic modulus by measuring the capsule shape and translational velocity, and the values were in good agreement with experimental data.

Although capillary flow can be used for measuring membrane mechanical properties, it is not applicable to measure the viscosity of the cytoplasm because the cell is just translated and any inner viscous effect must disappear. The viscosity

of the inner cytoplasm plays a key role in the dynamics of RBCs. Thus, other flow systems should be considered in evaluating the viscosity of the cytoplasm. One method for such an evaluation of viscosity is a micropore flow.

Thin pore flow has been investigated [7–10] because narrow geometry occurs in the human spleen. The spleen plays a role in the removal of aged RBCs [7,8] and increased cytoplasm viscosity has been suggested to be the dominant age-related mechanical change [10]. Freund [7] investigated the flow of RBCs numerically in a spleen-like thin slit. He found that RBC infolding occurs within the slit at high cytoplasm viscosity, and such infolding was suggested as a mechanism of jamming in the slit. The significance of cytoplasmic viscosity in a thin slit has been suggested, but it is unclear how the inner viscosity affects the flow field and how RBC motion changes with cytoplasmic viscosity. To fully understand the dynamics of RBCs in a micropore our theoretical understanding of pore flow should be enhanced.

In this study, we investigate the dynamics of an RBC in a thin micropore numerically, with various flow rates and viscosity ratios. In Sec. II, we describe the governing equations of fluid mechanics and membrane mechanics. For numerical simulations, we use a boundary element method for fluid mechanics and a finite element method for membrane mechanics. The numerical procedure is explained in Sec. III and the results are shown in Sec. IV. Finally, we conclude this study in Sec. V.

II. GOVERNING EQUATIONS

In this section, we describe the governing equations of fluid mechanics and membrane mechanics of RBCs in a pore flow. Because the basic equations of a capsule in a pore flow can be found in [3,6], we provide only a brief outline here.

A. Fluid mechanics

Consider an RBC passing through a thin micropore. We set a Cartesian frame (x, y, z) with the origin at the pore center (see Fig. 1). The flow direction is set along the x axis; thus, the micropore is set in the (y, z) plane. We define the inlet

*omori@pfs1.mech.tohoku.ac.jp

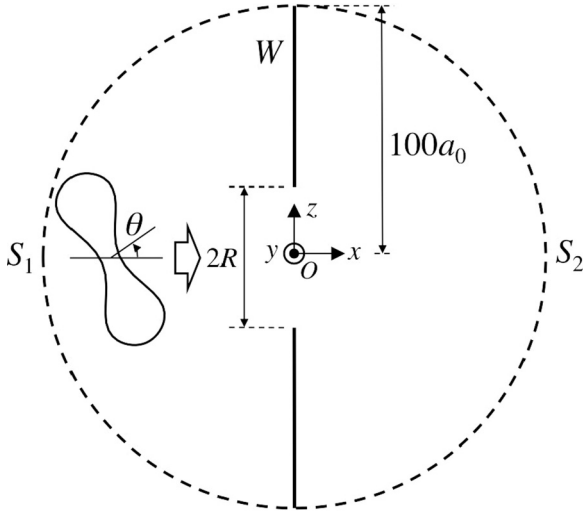


FIG. 1. Schematic illustration of an RBC in a thin micropore. W represents the wall boundary and S_1 and S_2 are inlet and outlet boundaries, respectively. a_0 is the radius of a spherical capsule, which has the same volume of an RBC.

and outlet boundaries as S_1 and S_2 , respectively, and the boundary conditions, including wall boundary W , are given by the following.

(1) No flow disturbance on S_1 and S_2 since they far are enough from an RBC

$$\mathbf{v}(\mathbf{x}) = \mathbf{v}^\infty(\mathbf{x}), \quad \mathbf{x} \in S_1 \cup S_2, \quad (1)$$

where \mathbf{v}^∞ is the undisturbed background flow.

(2) The pressures at S_1 and S_2 are given by

$$p(\mathbf{x}, t) = 0, \quad \mathbf{x} \in S_1, \quad (2)$$

$$p(\mathbf{x}, t) = \Delta p^\infty + \Delta p, \quad \mathbf{x} \in S_2, \quad (3)$$

where Δp^∞ is the pressure drop between S_1 and S_2 in the absence of an RBC and Δp is the additional pressure drop due to the RBC motion and deformation.

(3) No slip on the wall boundary W , i.e., $\mathbf{v}(\mathbf{x}) = \mathbf{0}$; $\mathbf{x} \in W$.

The Reynolds number, based on the characteristic length of cell dimensions, 8 [μm], a fast flow speed of 1 [mm/s], and plasma viscosity 1 [mPa s] is estimated as $\text{Re} < 10^{-2}$. We thus assume the flow is governed by the Stokes flow equation and the flow field is given by a boundary integral formulation [3,6]

$$\begin{aligned} \frac{1+\lambda}{2}\mathbf{v}(\mathbf{x}) = & \mathbf{v}^\infty(\mathbf{x}) - \frac{1}{8\pi\mu} \left[\int_A \mathbf{J}(\mathbf{x}, \mathbf{y}) \cdot \mathbf{q}(\mathbf{y}) dS(\mathbf{y}) \right. \\ & + \int_W \mathbf{J}(\mathbf{x}, \mathbf{y}) \cdot \mathbf{f}(\mathbf{y}) dS(\mathbf{y}) \\ & \left. - \Delta p \int_{S_2} \mathbf{J}(\mathbf{x}, \mathbf{y}) \cdot \mathbf{n}(\mathbf{y}) dS(\mathbf{y}) \right] \\ & + \frac{1-\lambda}{8\pi} \int_A^{PV} \mathbf{v}(\mathbf{y}) \cdot \mathbf{K}(\mathbf{x}, \mathbf{y}) \cdot \mathbf{n}(\mathbf{y}) dS(\mathbf{y}), \end{aligned} \quad (4)$$

where μ is the viscosity of the surrounding liquid, \mathbf{q} is the membrane load, \mathbf{f} is the wall friction, \mathbf{n} is a unit outward

normal vector, and \mathbf{J} and \mathbf{K} are single- and double-layer potentials of the Green's function, respectively [3]. Subscript A in the integral equation indicates the membrane surface of an RBC and the viscosity of the cytoplasm is described by $\lambda\mu$. PV denotes the principal value, defined as the value of the improper double-layer integral when the point \mathbf{x} is right on A . The additional pressure drop Δp is given by applying the reciprocal theorem to the flow without RBC ($\mathbf{v}^\infty, \boldsymbol{\sigma}^\infty$) and to the flow with an RBC ($\mathbf{v}, \boldsymbol{\sigma}$) in the domain bounded by $S_1 \cup S_2 \cup W \cup A$ [6], where $\boldsymbol{\sigma}$ and $\boldsymbol{\sigma}^\infty$ are the stress tensor with and without RBC, respectively. Assume that the flow rate Q does not change regardless of the RBC; the additional pressure drop can be determined by the following equation [3]:

$$\Delta p = \frac{1}{Q} \left[\int_A \mathbf{v}^\infty \cdot \mathbf{q} dS + (\lambda - 1) \int_A \mathbf{v} \cdot \boldsymbol{\sigma}^\infty \cdot \mathbf{n} dS \right]. \quad (5)$$

B. Membrane mechanics

Next, we derive the membrane mechanics of an RBC. An RBC is modeled as a capsule with a hyperelastic thin membrane, which has a surface shear elastic modulus G_s and area-dilation modulus K_s . Because the membrane thickness is very small compared to the characteristic cell size and its typical radius of curvature, we consider only the deformation in the median surface, devoid of bending resistance. In this case, the stress can be integrated towards the thickness direction and be replaced by tension (force per unit arch length). We use the Skalak constitutive law [9] for the membrane, which can independently express the large elastic deformation and strong area-dilation resistance of the membrane. The two-dimensional principal tensions of the Skalak law, τ_1 and τ_2 , are given by

$$\tau_1 = \frac{G_s \lambda_1}{\lambda_2} (\lambda_1^2 - 1 + C \lambda_2^2 (\lambda_1^2 \lambda_2^2 - 1)) \quad (\text{likewise for } \tau_2), \quad (6)$$

where λ_1 and λ_2 are the principal stretch ratios. The material parameter C is defined as $K_s = G_s(1 + 2C)$. To express an incompressible property of a biological membrane, C must be large enough. In our former study [11], we investigated the effect of C and found that a value of $C = 10$ was high enough to express the incompressibility of a biological membrane. Thus, we used $C = 10$ in all simulations.

To couple the fluid mechanics and membrane mechanics, we need to calculate the force equilibrium between the internal elastic tension $\boldsymbol{\tau}$ and the exerted fluid viscous traction force \mathbf{q} . Neglecting any inertia effect of the membrane motion, the equilibrium equation of the membrane in the weak form is given by [12]

$$\int_A \hat{\mathbf{u}} \cdot \mathbf{q} dS = \int_A \hat{\boldsymbol{\epsilon}} : \boldsymbol{\tau} dS, \quad (7)$$

where $\hat{\mathbf{u}}$ and $\hat{\boldsymbol{\epsilon}}$ are the virtual displacement and strain, respectively.

We introduce an important nondimensional parameter, the capillary number, which represents the ratio between the fluid viscous traction force and the elastic resistance of

the membrane. The capillary number is defined as

$$\text{Ca} = \frac{\mu Q}{a_0^2 G_s}, \quad (8)$$

where a_0 is the volume equivalent radius of an RBC, which is estimated as $a_0 = 2.82$ [μm] [13]. In capillary blood vessels, the mean blood flow velocity ranges from 0.1 to 1 [mm/s] [14]. If we assume $G_s = 4$ [$\mu\text{N/m}$] [7], the capillary number would be 0.1 to 1. To cover the physiological range of the capillary number in capillary blood vessels, Ca is set to 0.1 to 2 in this study.

III. NUMERICAL METHOD

In this section, we explain the numerical method. Because the methodology of our numerical scheme has already been reported by the authors of [11,15,16], we provide only a brief outline here.

We track a Lagrangian material point of the RBC membrane $\mathbf{x}(t); \mathbf{x} \in A$ over time. Thus, we can readily compute local membrane deformation by comparison to its reference state. Using the membrane constitutive law, we can compute the in-plane tension $\boldsymbol{\tau}$ in each time step. We next solve the equilibrium Eq. (7) with respect to membrane load \mathbf{q} using a finite element method [11,12]. Then, we calculate the additional pressure drop Δp by solving Eq. (5). Now that the load \mathbf{q} and the pressure drop Δp are known, the wall friction \mathbf{f} can be computed by the application of Eq. (4) to $\mathbf{x} \in W$ as follows:

$$\begin{aligned} & \int_W \mathbf{J}(\mathbf{x}, \mathbf{y}) \cdot \mathbf{f}(\mathbf{y}) dS(\mathbf{y}) \\ &= - \int_A \mathbf{J}(\mathbf{x}, \mathbf{y}) \cdot \mathbf{q}(\mathbf{y}) dS(\mathbf{y}) + \Delta p \int_{S_2} \mathbf{J}(\mathbf{x}, \mathbf{y}) \cdot \mathbf{n}(\mathbf{y}) dS(\mathbf{y}) \\ & \quad + (1 - \lambda)\mu \int_A \mathbf{v}(\mathbf{y}) \cdot \mathbf{K}(\mathbf{x}, \mathbf{y}) \cdot \mathbf{n}(\mathbf{y}) dS(\mathbf{y}). \end{aligned} \quad (9)$$

Because the boundary wall $\mathbf{x} \in W$ is independent of time, the linear system (9) is solved by multiplying the right-hand side by the inverse coefficient matrices of \mathbf{f} , which is calculated preliminarily. Velocity \mathbf{v} is then updated by solving the boundary integral Eq. (4). In nonuniform viscosity ratio cases, the velocity \mathbf{v} must be solved implicitly; i.e., Eqs. (4), (5), and (9) must be solved as a system equation. We use a similar numerical scheme to that of Foessel *et al.* [17]; the velocity \mathbf{v} is computed by a simple iteration scheme. Once the velocity \mathbf{v} is updated, the membrane material point $\mathbf{x} \in A$ is also updated by means of the nonslip condition on the membrane wall $d\mathbf{x}/dt = \mathbf{v}$, which is solved by a second-order Runge-Kutta time-marching method. The above computational procedure is then repeated until sufficient data are obtained.

To discretize the RBC membrane, we use a subdividing method in the same manner as the authors of [12]. The first mesh is constructed as an icosahedron with 20 regular triangles. A new computational node is placed at the middle of each edge; therefore, each triangle element is divided into four new elements. The new nodes are projected onto the sphere with a radius a_0 and the procedure is repeated until the desired number of elements is reached.

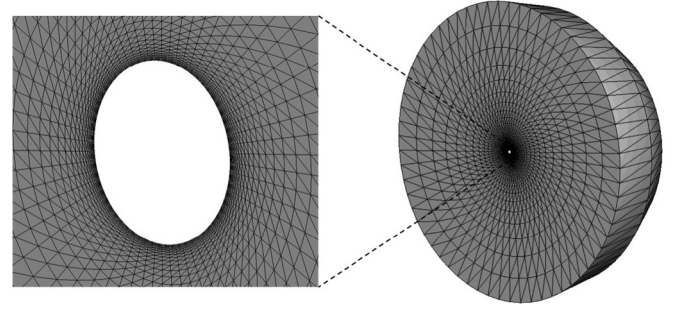


FIG. 2. Computational meshes of the wall boundary W and outlet boundary S_2 . Mesh resolution of the wall boundary becomes larger as it approaches the pore.

The biconcave disk shape, which is assumed as the reference shape of the RBC, is given in the same manner as found in [13]. The computational node $\mathbf{x}(X, Y, Z)$ is initially generated on a spherical surface, then projected onto the derived biconcave shape \mathbf{x}^{rbc} by using the following transformation functions:

$$\begin{aligned} X^{\text{rbc}} &= \frac{a}{a_0} X, \\ Y^{\text{rbc}} &= \pm \frac{1}{2} a (1 - r^2)^{1/2} (C_0 + C_2 r^2 + C_4 r^4), \\ Z^{\text{rbc}} &= \frac{a}{a_0} Z, \end{aligned} \quad (10)$$

where $r^2 = (X^2 + Z^2)/a_0^2$ and a is the radius of the biconcave disk. The plus sign in the second term is for $Y > 0$ (likewise for the minus sign). C_0 , C_2 , and C_4 are the shape parameters to control the swelling ratio of the biconcave shape. To coincide with the shape as in the physiological condition, these parameters are set to $C_0 = 0.207$, $C_2 = 2.003$, and $C_4 = -1.123$, respectively [13]. For the volume conservation, a_0 and a need to satisfy the correlation $a = 1.386a_0$.

The initial orientation of the RBC is described by θ , defined as the angle between the x axis and the revolution axis of the biconcave disk, as shown in Fig. 1. For simplicity, the initial position of the cell is set to $(x_g/a_0, y_g/a_0, z_g/a_0) = (-3.0, 0, 0)$ in all cases, where \mathbf{x}_g is the mass center of the RBC.

The computational domain is shown in Figs. 1 and 2. To eliminate the flow disturbance on the inlet and outlet boundaries, they must be set far enough from the micropore. In this study, S_1 and S_2 are set at the position of $100a_0$ from the pore center, as shown in Fig. 1. The pore radius R is set as $R/a_0 = 1.2$ or $R/a_0 = 1.5$. These values are equivalent to $R/a \approx 0.87$ and $R/a \approx 1.08$, respectively, where a is the half major axis length of the biconcave disk. The computational meshes of W and S_2 are shown in Fig. 2. The mesh resolution of the wall boundary becomes larger as it approaches the pore. The finest mesh size is about $(dS_e)^{0.5} = 0.02a_0$, where dS_e is the area of the triangle element. For time convergence, the time step size Δt ranges from 1.0×10^{-5} to 1.0×10^{-3} in this study.

IV. RESULTS AND DISCUSSION

A. Motion and deformation of the RBC

Typical results of the RBC in the pore flow are shown in Fig. 3. The capillary number Ca is set to 0.3 [Fig. 3(a)] and

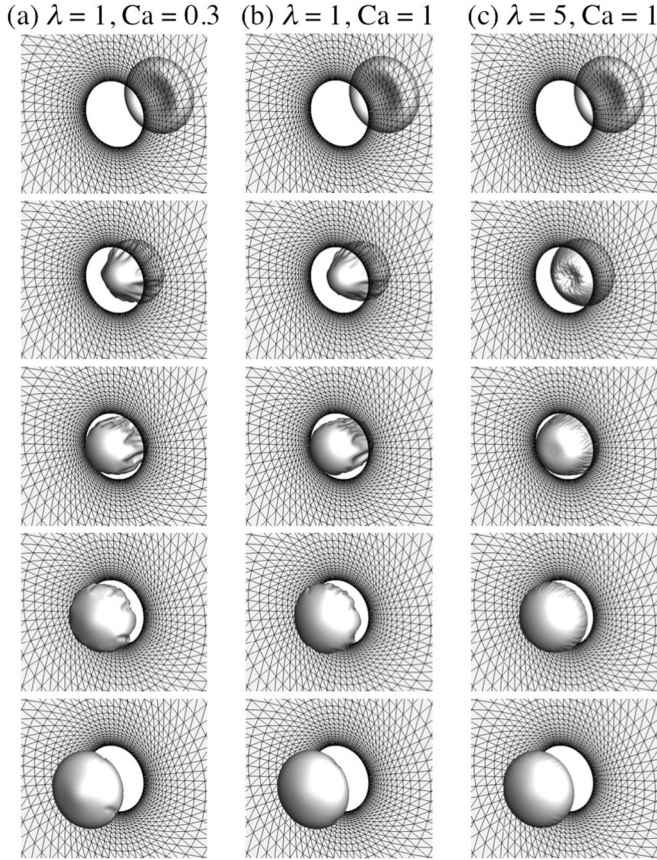


FIG. 3. Time sequence of the RBC passing through the micropore with $Ca = 0.3, 1$ and $\lambda = 1, 5$. The pore size is $R/a_0 = 1.2 (R/a \approx 0.87)$.

1.0 [Figs. 3(b) and 3(c)]. The pore radius R is $R/a_0 = 1.2$ in all three cases. As the RBC moves closer to the pore, the front side of the cell membrane is gradually elongated in the flow direction, whereas the rear side remains a dimple structure. To pass the narrow pore, the RBC is forced to compress towards the pore radius direction, and we observe membrane folding around the side rim, while membrane folding does not occur at the front edge of the cell. This tendency is similar to the result of a capsule in a narrow tube [6]. After the passing, the RBC shape gradually becomes a parachute shape, and it reaches a steady state when $x_g \geq 1.5$. Figure 4 shows the two-dimensional (2D) cell profile of Figs. 3(b) and 3(c). We see that the deformation towards the flow direction increases as λ decreases, while the distance between the wall edge and the membrane decreases as λ increases.

To calculate RBC deformation more quantitatively, we measure the axis length of the RBC. We define L_{fr} as the length between the front-to-rear edge in the x axis (cf. Fig. 4). We also define L_x as the maximum length in the (x, z) plane. The length is measured when $x_g = 0$ in all cases. We found that L_x increases monotonically as Ca increases, while L_{fr} shows almost plateau curves when $Ca \geq 1$ [cf. Fig. 5(a)]. We also see that the curves of $R/a_0 = 1.2$ are always higher than the curves of $R/a_0 = 1.5$. The effect of λ is also shown in Fig. 5(b). Both L_{fr} and L_x decrease monotonically as λ decreases. By comparing Figs. 5(a) and 5(b), we find that RBC deformations

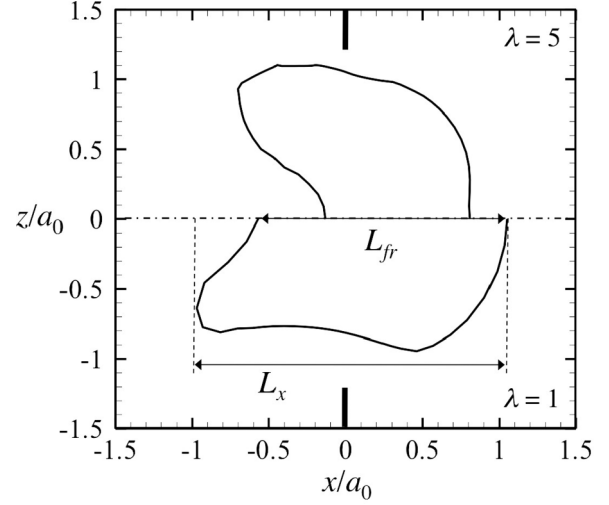


FIG. 4. Profile of the RBC in the (x, z) plane when $x_g = 0$. $\lambda = 1$ (bottom) and 5 (top), and $Ca = 1$ in both cases.

are changed considerably by λ , whereas they are moderately affected by changing Ca . This suggests that RBC deformation tends to be prevented by high λ .

We next measure the radial deformation of the RBC; the results are shown in Fig. 6. As with L_x , the RBC shape in the (y, z) plane is significantly changed by λ . In a small λ condition, we observe strong membrane compression and large wrinkles are observed at the side rim [cf. Fig. 6(a)]. We also measure the gap between the wall edge and the cell membrane, defined as

$$\Delta r = \min_{t \in T} (R - r_{ave}), \quad (11)$$

where T is the passage of time and r_{ave} is defined as

$$r_{ave} = \frac{1}{N} \sum_i^N \|x^i\| \quad \text{with } x^i (x^i = 0, y^i, z^i).$$

N is the number of nodes on the membrane with $x = 0$. The results are shown in Fig. 6(b). Δr decreases with λ but the value does not reach zero, meaning the membrane does not touch the wall edge. The small gap between the cell and the wall is likely the cause of the large pressure drop; thus, a high λ condition may yield strong flow resistance. For a more detailed analysis

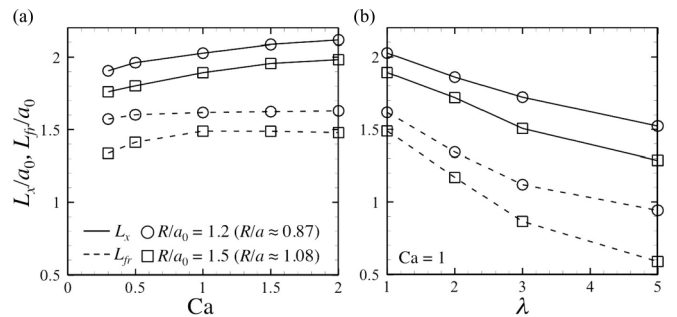


FIG. 5. The axial length L_{fr} and the maximum length L_x with various Ca and λ . In panel (a), the viscosity ratio λ is set to unity in all cases, while $Ca = 1$ in panel (b).

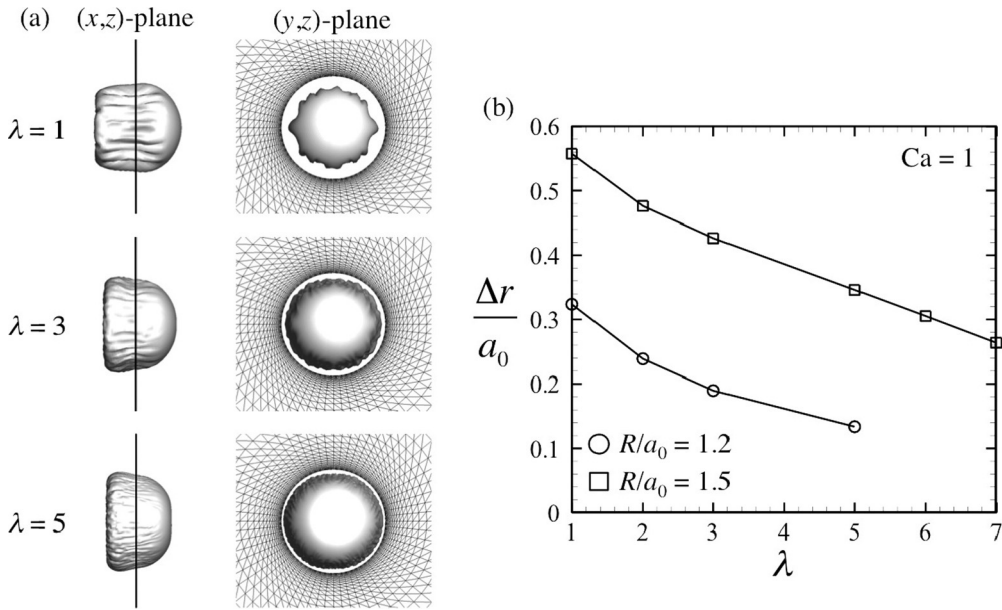


FIG. 6. RBC deformation in the (y,z) plane. (a) RBC profiles in the (x,z) and (y,z) planes when $x_g = 0$ ($Ca = 1$, $R/a_0 = 1.2$, and $\theta = 0$). (b) Δr with $R/a_0 = 1.2$ and $R/a_0 = 1.5$.

of the flow field, we next investigate the additional pressure drop Δp with various Ca and λ conditions.

B. Pressure drop

In Fig. 7(a), the time change of Δp with different Ca is shown. Ca is set as $Ca = 0.3, 0.5, 1.0, 1.5$ and 2.0 , and the viscosity ratio λ is equal to 1. We see that Δp increases rapidly as the RBC approaches the pore. In the early stage of passage, Δp becomes the maximum. At the same time, L_x also reaches a maximum value [cf. Fig. 7(b)]. In the case of $\lambda = 1$, Δp is determined only by the membrane load q [cf. Eq. (5)]. The load q is calculated by the cell deformation; thus, the additional pressure drop is relevant to the cell deformation. This tendency is clearly observed in high Ca conditions. Once Δp reaches the maximum, both Δp and L_x decrease with time. After the end of the passage, the RBC gradually recovers from its compressed bullet shape to a free parachute shape. In this recovery sequence, Δp shows small oscillations. When the

cell is far enough from the pore, the shape reaches a steady state and Δp is asymptotic to zero.

We next investigate the effect of the initial orientation θ . Figure 8 shows the shape profile and the additional pressure drop with $\theta = \pi/4$ and $\pi/2$. As with $\theta = 0$ cases (i.e., Fig. 7), the cell is compressed towards the radial direction to pass through the pore [see Fig. 8(a)]. After passing, the RBC shape changes gradually to a parachute shape, and reaches a steady state when the cell is far enough away from the pore. The time change in the pressure drop is shown in Fig. 8. The maximum value of Δp does not change much with the changes in θ .

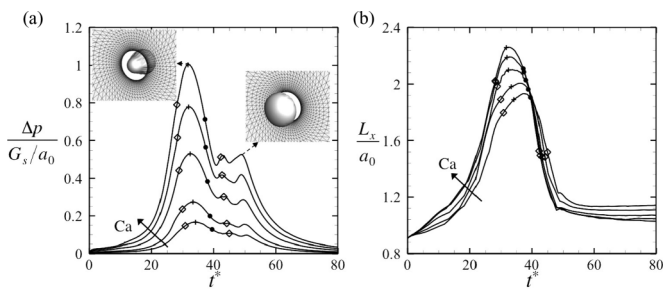


FIG. 7. Additional pressure drop with various Ca conditions. Ca is set as $0.3, 0.5, 1.0, 1.5$, and 2.0 . In all cases, the viscosity ratio is set 1.0. The definition of the symbols appearing in the figure are as follows. \diamond : start or end time of the passage event; \bullet : time at $x_g = 0$; and $+$: time at Δp becomes the maximum. Nondimensional time t^* is defined as $t^* = t Q/a_0^3$.

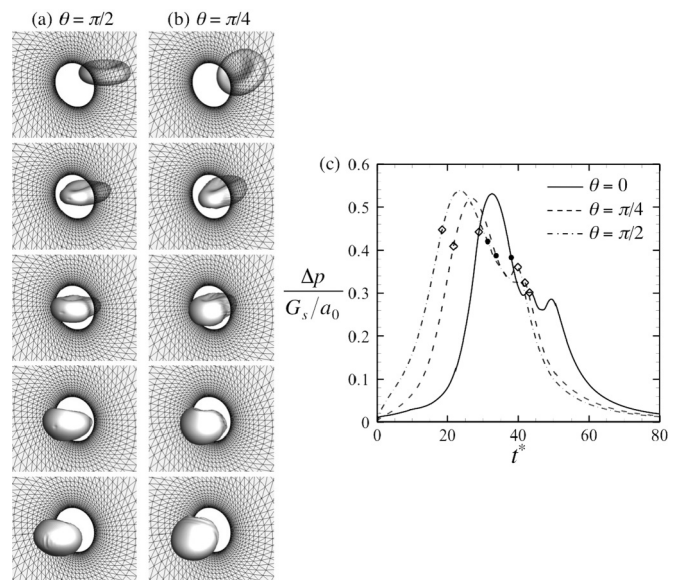


FIG. 8. Δp with different initial orientation θ . $\lambda = 1$ and $R/a_0 = 1.2$. Symbols in panel (b) are the same as in Fig. 7.

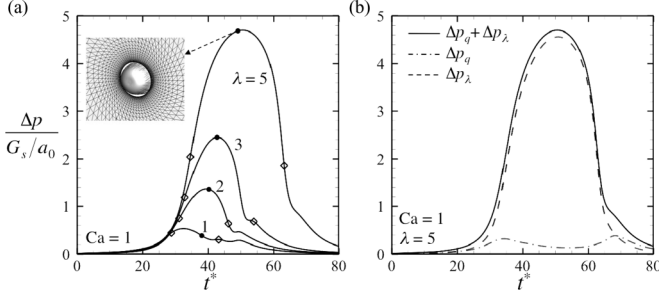


FIG. 9. Time change of Δp with various λ . The cell shape at $x_g = 0$ is inserted in panel (a). Symbols in the figure are the same as in Figs. 7 and 8.

The time change of Δp with various λ is also shown in Fig. 9(a). This figure clearly shows that the time average and the maximum Δp become larger as λ increases. The maximum Δp appears when $x_g = 0$, which is different from the previous unity viscosity ratio cases. To investigate the λ effect in more detail, Eq. (5) is divided into two components: Δp_q and Δp_λ . Δp_q is the first term of Eq. (5), based on deformation effects, because it is determined by the membrane load \mathbf{q} . We also define Δp_λ as the second term of Eq. (5). Δp_λ is determined by λ and velocity \mathbf{v} ; thus, it can be seen as the viscous effect on the pressure drop. We note Δp_λ disappears when $\lambda = 1$. Δp_q and Δp_λ of $\lambda = 5$ are shown in Fig. 9(b). We see that Δp is dominated by Δp_λ , and Δp_λ is almost 30 times larger than Δp_q at most. This indicates that Δp is determined mainly by Δp_λ , not by Δp_q , when $\lambda = 5$.

We also calculate the time average pressure drop. The time average Δp is calculated as

$$\Delta \bar{p} = \frac{1}{T_{\text{out}} - T_{\text{in}}} \int_{T_{\text{in}}}^{T_{\text{out}}} \Delta p dt, \quad (12)$$

where

$$T_{\text{in}} = t(\max_{x \in A} x = 0), \quad T_{\text{out}} = t(\min_{x \in A} x = 0),$$

and the results are shown in Fig. 10(a). From this figure, we see that time average pressure drop $\Delta \bar{p}$ increases almost linearly with λ . Also, its slope increases as Ca increases. Accordingly, $\Delta \bar{p}$ becomes higher in a high λ and Ca regime.

In Fig. 10(b), the maximum pressure drop during the passage is shown. We see that the pressure drop increases linearly with the capillary number. This result indicates that

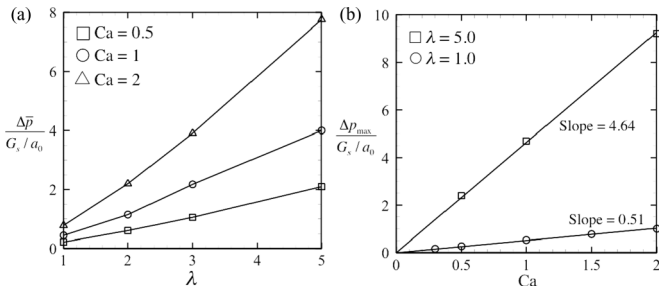


FIG. 10. (a) Time average pressure drop. (b) Maximum pressure drop. Lines with slope equal to 0.51 and 4.64 are drawn for comparison to those found in [18].

the additional pressure drop is proportional to the flow rate Q since the capillary number is defined as $Ca = \mu Q / G_s a_0^2$. This tendency is the same as the previous experiments found in [19,20]. We also compare our results to the results of channel flow [18]. In the paper of Abkarian *et al.* [18], they used a rectangular channel with $5 \times 5 \mu\text{m}$ in the cross section. Using the theory of capillary flow [21], they estimated the maximum additional pressure drop as $\Delta p_{\text{max}} = 16\mu V / R$, where V is the mean velocity of the fluid flow. To compare our results to the experimental results, we derive the relation between Δp_{max} and $\mu V / R$ as follows.

In this study, Δp_{max} is normalized by the membrane elastic shear modulus G_s and the length of the cell a_0 : $\Delta p_{\text{max}}^* = \Delta p_{\text{max}} a_0 / G_s$. Thus the ratio between Δp_{max}^* and Ca can be written as

$$\frac{\Delta p_{\text{max}}^*}{Ca} = \frac{\Delta p_{\text{max}} a_0^3}{\mu Q}. \quad (13)$$

Using the relation of $Q = \pi R^2 V$, the above equation can be rewritten as

$$\Delta p_{\text{max}} = \pi \left(\frac{R}{a_0} \right)^3 \frac{\Delta p_{\text{max}}^* \mu V}{Ca R}. \quad (14)$$

As shown in Fig. 10(b), $\Delta p_{\text{max}}^* / Ca$ becomes about 0.51 when $\lambda = 1$ and 4.64 when $\lambda = 5$. Substituting $R/a_0 = 1.2$ and the results of $\Delta p_{\text{max}}^* / Ca$ into Eq. (14), we have

$$2.77 \leq \Delta p_{\text{max}} R / \mu V \leq 25.2 \quad \text{with } \lambda \in [1, 5]. \quad (15)$$

This is in agreement with the order of magnitude from the results of Abkarian *et al.*, though the geometries of the two studies are completely different. These results suggest that the effect of the pore length would be small or moderate on the additional pressure drop, and the additional pressure drop tends to be proportional to flow rate regardless of the pore thickness.

C. Passage time

In this section, we discuss the transit time of the RBC passing through the micropore. The passage time is defined as

$$T = T_{\text{out}} - T_{\text{in}}, \quad (16)$$

and normalized by $T^* = T Q / a_0^3$. Nondimensional passage time T^* as a function of Ca is shown in Fig. 11(a). The initial

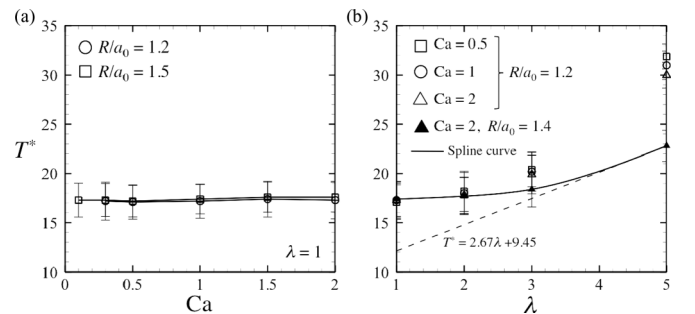


FIG. 11. Nondimensional passage time with different Ca and λ . The data obtained from various θ cases. Error bars in the figure represent standard deviation.

angle is set as $\theta = 0, \pi/6, \pi/3$, and $\pi/2$, and the average T^* is plotted in the figure. In Fig. 11(a), we see that T^* is independent of Ca in both $R/a_0 = 1.2$ and $R/a_0 = 1.5$ cases, suggesting that transit time T is proportional to Q^{-1} . T^* as a function of λ is also shown in Fig. 11(b), and we clearly see that T^* increases nonlinearly with respect to λ . To investigate the effect of λ in more detail, we conduct a simple scaling analysis below.

When $\lambda \ll 1$, the effect of cytoplasm viscosity can be omitted and transit time is simply scaled by the characteristic length a_0 and velocity V : $T \sim a_0/V = \pi R^2 a_0/Q$. When $\lambda \gg 1$, the effect of cytoplasm viscosity becomes dominant and the transit time should be determined by the rate of strain $T \propto \dot{\gamma}^{-1}$. In high λ conditions, $\dot{\gamma}$ may be estimated by $\dot{\gamma} \sim \tau/\mu_{in}$, where the driving stress is τ and the inner viscosity μ_{in} . Assume that the driving stress is scaled by $\tau \propto \mu_{out} Q/a_0^3$, and we have $\dot{\gamma} \propto Q/(\lambda a_0^3)$. Using the inverse relationship between transit time and strain rate, the transit time can be described as

$$T \propto \dot{\gamma}^{-1} = \frac{\lambda a_0^3}{Q}.$$

Then, nondimensional transition time TQ/a_0^3 may be proportional to λ when $\lambda \gg 1$. In a $\lambda \sim 1$ regime, the transition regime from the small λ region to the high λ region can be seen, and the transit time can change nonlinearly with respect to λ , as shown in Fig. 11(b).

In conclusion, transit time and pressure drop are strongly dependent on the viscosity ratio λ . This result could be used to evaluate the viscosity of the inner liquid. To demonstrate how the result can be used to evaluate the cytoplasmic viscosity, we roughly compare transit time to the experimental data from Cokelet [19]. Cokelet investigated RBC motion in a

micropore and measured the transit time by a simple mass balance theory. Typical experimental data from the paper can be written as $R/a_0 = 1.42$, $Q = 7.5 \times 10^{-14} [\text{m}^3/\text{s}]$ and $T^* = 24.7$. If we assume the membrane shear elastic modulus $G_s = 4.0 [\mu\text{N}/\text{m}]$ and the suspending medium viscosity $\mu = 1 [\text{mPa s}]$ (phosphate buffered saline with 0.5% albumin was used in the experiment), the capillary number in the experiment can be evaluated as $\text{Ca} \approx 2.35$. For comparison, our numerical results of $\text{Ca} = 2.0$ and $R/a_0 = 1.4$ are plotted in Fig. 11(b). We assume that the transit time is proportional to λ when $\lambda \geq 5$, and the slope is evaluated from a cubic spline curve at $\lambda = 5$ [cf. Fig. 11(b)]. The fitting line can be written as $T^* = 2.67\lambda + 9.45$, and $T^* = 24.7$, giving us $\lambda = 5.7$. We again assume that the medium viscosity is 1 [mPa s], the cytoplasm viscosity can be estimated as 5.7 [mPa s]. Because the cytoplasmic viscosity of a fresh RBC is about 6 [mPa s] [7], the value of 5.7 [mPa s] seems reasonable.

V. CONCLUSION

In this study, we investigate an RBC passage through a thin micropore numerically. We found that RBC deformation tends to be suppressed by high λ , and the additional pressure drop Δp rapidly increases with λ . As a result, the transit time increases nonlinearly in the moderate λ regime, whereas it is almost invariant with Ca. From these results, we conclude the viscosity ratio between the inner and outer liquids plays a significant role when RBCs pass through a micropore. Because the inner viscosity of RBCs increases with cell age, these λ effects might be helpful for filtering in the splenic sinus *in vivo*. The results described here may be useful for designing a microfluidic device to measure the cytoplasm viscosity of RBCs, which is difficult to evaluate using capillary flow.

-
- [1] T. W. Secomb, R. Skalak, N. Ozkaya, and J. F. Gross, *J. Fluid Mech.* **163**, 405 (1986).
 - [2] J. B. Freund and M. M. Orescanin, *J. Fluid Mech.* **671**, 466 (2011).
 - [3] C. Pozrikidis, *Ann. Biomed. Eng.* **33**, 165 (2005).
 - [4] A. R. Pries, D. Neuhaus, and P. Gaetgens, *Am. J. Physiol. Heart Circ. Physiol.* **263**, H1770 (1992).
 - [5] G. Tomaiuolo and S. Guido, *Microvasc. Res.* **82**, 35 (2011).
 - [6] X. Q. Hu, A. V. Salsac, and D. Barthès-Biesel, *J. Fluid Mech.* **705**, 176 (2011).
 - [7] J. B. Freund, *Phys. Fluids* **25**, 110807 (2013).
 - [8] I. C. MacDonald, D. M. Ragan, E. E. Schmidt, and A. C. Groom, *Microvasc. Res.* **33**, 118 (1987).
 - [9] R. Skalak, A. Tozeren, R. P. Zarda, and S. Chien, *Biophys. J.* **13**, 245 (1973).
 - [10] T. Shiga, M. Sekiya, N. Maeda, K. Kon, and M. Okazaki, *Biochim. Biophys. Acta.* **814**, 289 (1985).
 - [11] T. Omori, Y. Imai, T. Yamaguchi, and T. Ishikawa, *Phys. Rev. Lett.* **108**, 138102 (2012).
 - [12] J. Walter, A.-V. Salsac, D. Barthès-Biesel, and P. L. Tallec, *Int. J. Numer. Meth. Eng.* **83**, 829 (2010).
 - [13] E. A. Evans and Y. C. Fung, *Microvasc. Res.* **4**, 335 (1972).
 - [14] T. J. Pedley, *The Fluid Mechanics of Large Blood Vessels* (Cambridge University Press, Cambridge, England, 1980).
 - [15] T. Omori, T. Ishikawa, D. Barthès-Biesel, A.-V. Salsac, Y. Imai, and T. Yamaguchi, *Phys. Rev. E* **86**, 056321 (2012).
 - [16] T. Omori, T. Ishikawa, Y. Imai, and T. Yamaguchi, *J. Fluid Mech.* **724**, 154 (2013).
 - [17] E. Foessel, J. Walter, A.-V. Salsac, and D. Barthès-Biesel, *J. Fluid Mech.* **672**, 477 (2011).
 - [18] M. Abkarian, M. Faivre, and H. A. Stone, *Proc. Natl. Acad. Sci. U.S.A.* **103**, 538 (2006).
 - [19] G. Cokelet, *Scand. J. Clin. Lab. Invest. Suppl.* **156**, 77 (1981).
 - [20] D. Koutsouris, M. Hanss, and R. Skalak, *Biorheology* **20**, 779 (1983).
 - [21] C. Queguiner and D. Barthès-Biesel, *J. Fluid Mech.* **348**, 349 (1997).